nature microbiology

SUPPLEMENTARY INFORMATION

https://doi.org/10.1038/s41564-018-0128-4

In the format provided by the authors and unedited.

Coccolithovirus facilitation of carbon export in the North Atlantic

Christien P. Laber[1], Jonathan E. Hunter[2], Filipa Carvalho[1,8], James R. Collins[2], Elias J. Hunter[1], Brittany M. Schieler[1], Emmanuel Boss[3], Kuldeep More[4], Miguel Frada[5,9], Kimberlee Thamatrakoln[1], Christopher M. Brown[1], Liti Haramaty[1], Justin Ossolinski[2], Helen Fredricks[2], Jozef I. Nissimov[1], Rebecca Vandzura[1,10], Uri Sheyn[5], Yoav Lehahn[5,11], Robert J. Chant[1], Ana M. Martins[6], Marco J. L. Coolen[4], Assaf Vardi[5], Giacomo R. DiTullio[7], Benjamin A. S. Van Mooy[2] and Kay D. Bidle[1]*

[1]Department of Marine and Coastal Sciences, Rutgers University, New Brunswick, NJ, USA. [2]Department of Chemistry and Geochemistry, Woods Hole Oceanographic Institution, Woods Hole, MA, USA. [3]School of Marine Sciences, University of Maine, Walpole, ME, USA. [4]Western Australian Organic and Isotope Geochemistry Center, Department of Chemistry, Curtin University, Bentley, WA, Australia. [5]Department of Plant and Environmental Sciences, Weizmann Institute of Science, Rehovot, Israel. [6]Department of Oceanography and Fisheries, University of the Azores, Faial, Azores, Portugal. [7]Grice Marine Laboratory, College of Charleston, Charleston, SC, USA. Present address: [8]National Oceanography Centre, Southampton, United Kingdom. [9]The Interuniversity Institute for Marine Sciences—Eilat, Eilat, Israel. [10]College of Earth, Ocean and Environment, University of Delaware, Newark, DE, USA. [11]Department of Marine Geosciences, University of Haifa, Haifa, Israel. *e-mail: bidle@marine.rutgers.edu

Coccolithovirus facilitation of carbon export in the North Atlantic
Supplementary Information

Christien P. Laber, Jonathan E. Hunter, Ana Filipa Carvalho, James R. Collins, Elias Hunter, Brittany Schieler, Emmanuel Boss, Kuldeep More, Miguel Frada, Kimberlee Thamatrakoln, Christopher M. Brown, Liti Haramaty, Justin Ossolinski, Helen Fredricks, Jozef I. Nissimov, Rebecca Vandzura, Uri Sheyn, Yoav Lehahn, Robert J. Chant, Ana M. Martins, Marco J. L. Coolen, Assaf Vardi, Giacomo R. DiTullio, Benjamin A.S. Van Mooy, and Kay D. Bidle

Supplemental Figures 1-15

Supplemental Tables 1-3

SUPPLEMENTAL FIGURES

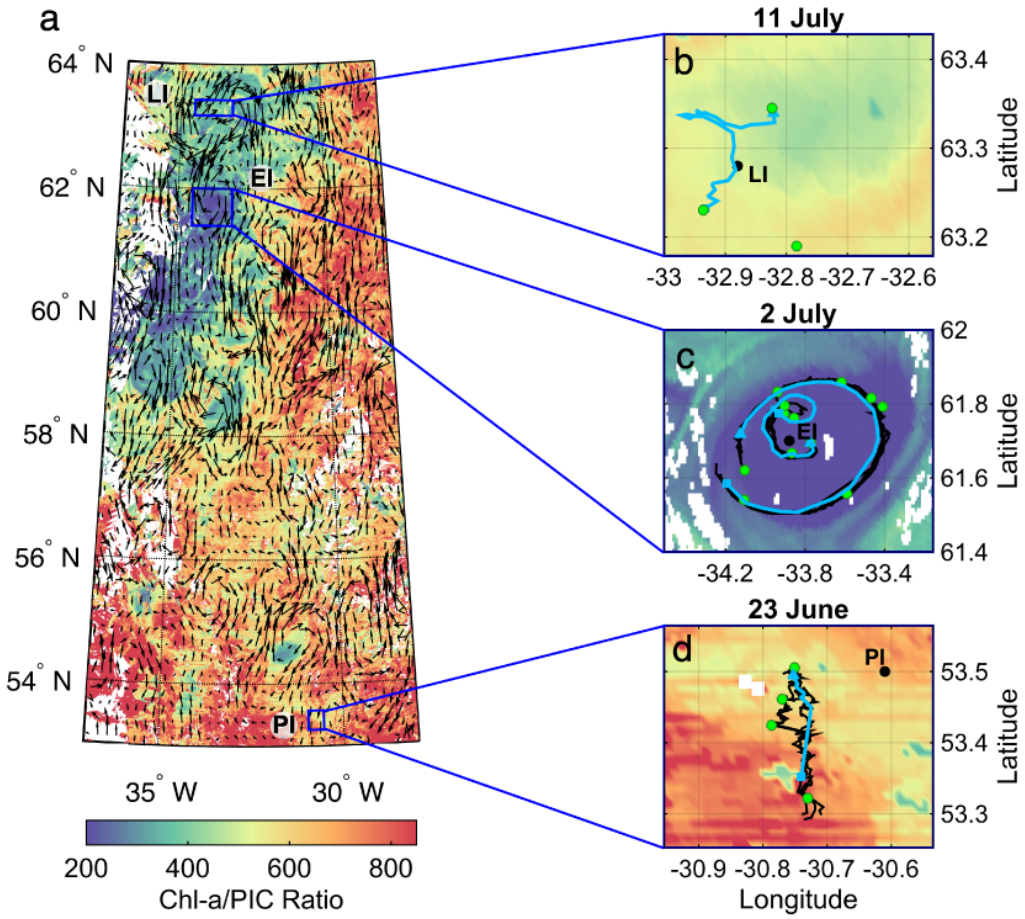

Supplemental Figure 1. Landscape of surface currents across the NA-VICE study region. (a) 18-day (23 June – 11 July) composite of Chlorophyll *a* (Chl *a*)/particulate inorganic carbon (PIC) ratio over the study region with an 8-day moving average altimetry overlay centered on June 23. Altimetry reveals the anticyclonic structure of EI and LI and the southward movement of PI. Profiling floats (blue) and sediment traps (black) deployed at LI (b), EI/ EI_R (c) and PI (d) closely followed the observed sea surface movement. Green markers indicate CTD cast locations. (a) The float and sediment traps at EI were deployed in the western side of the eddy. The float and traps traveled clockwise around the eddy, forming an almost complete circle upon recovery. Float and traps were deployed at EI_R near the center of the eddy feature and traveled with tighter clockwise movement before recovery. (b) The profiling float deployed at LI the traveled west before looping back south, remaining in the eddy for the duration of the deployment. No sediments traps were deployed at LI. (c) Float and sediment trap deployments at PI experienced coherent movement south of the deployment location. Triangles indicate float deployment location; squares indicate recovery. Note that color images in (b-d) are for illustrative purposes and correspond to satellite imagery for a specific day, while tracks of floats and sediment traps cover the 4-day deployment period. For (a), Chl *a*/PIC layer

pixels are n = 18, other than where covered by cloud. For (b-d), single day satellite products are n = 1.

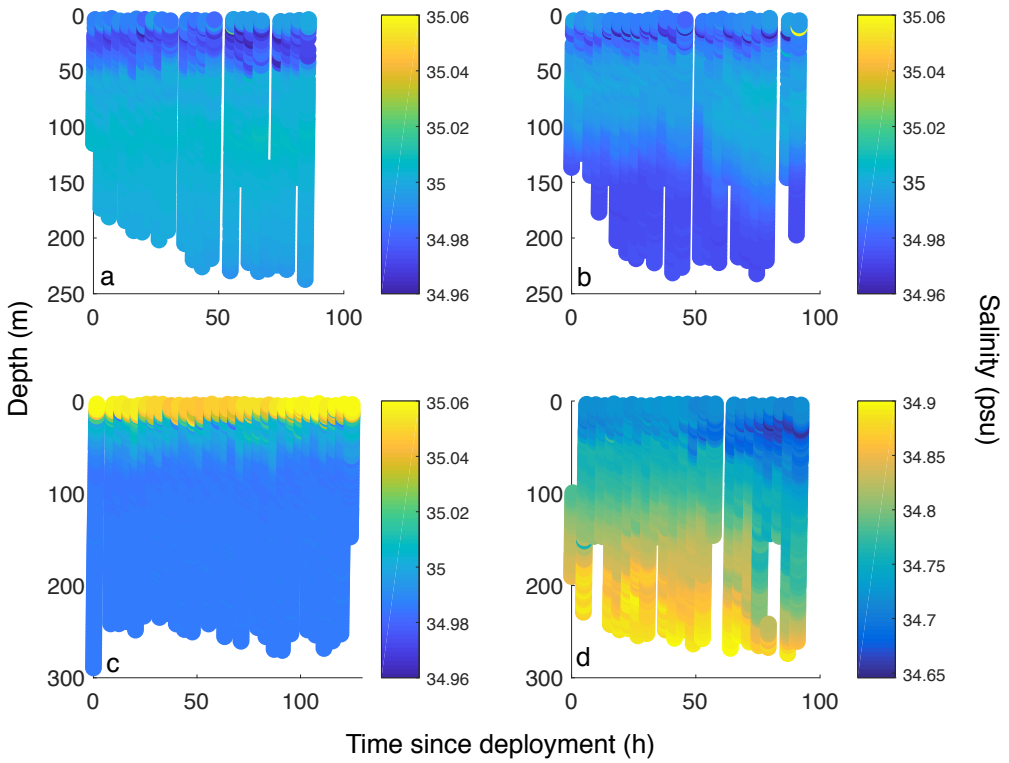

Supplemental Figure 2. Salinity profiles for EI (a), EI_R (b), LI (c), and PI (d) stations during float deployments. Salinity remained similar for individual depths at all stations except for PI, where decreases in salinity by 0.1 psu were observed below the surface layer between 50-74 h. These observations are consistent with mixing water masses. The consistency of flow cytometry data, along with lipid- and gene-based measurements, before and after this incursion suggests that Lagrangian sampling was maintained in the surface waters. Color bars all scaled similarly except for D. For each data point, *n* = 1 technical replicate.

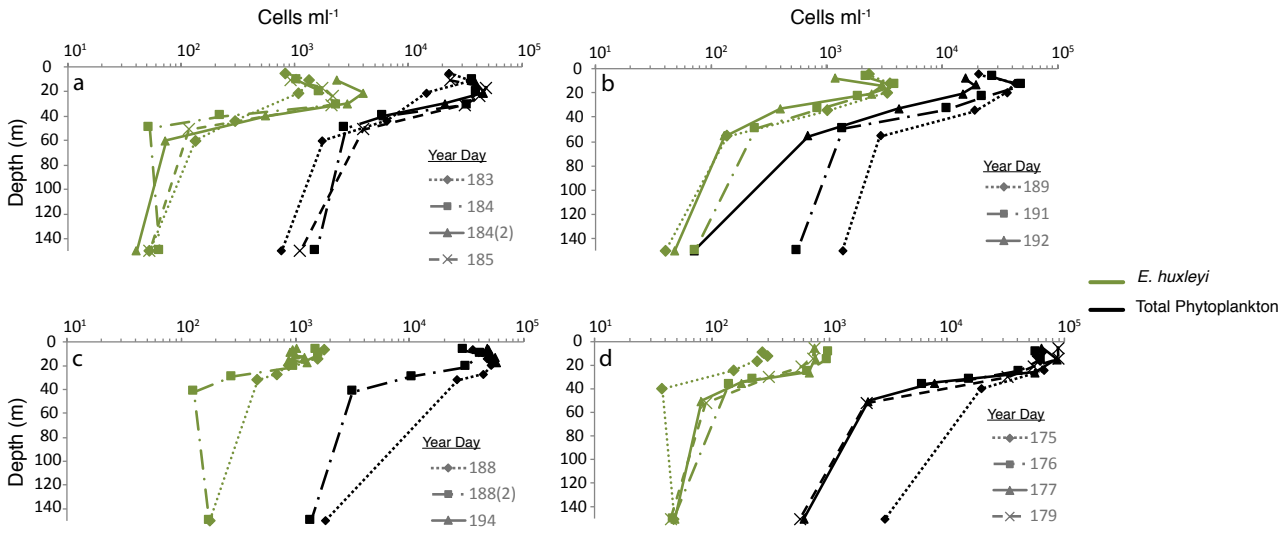

Supplemental Figure 3.Flow cytometry counts of *E. huxleyi* (green) and all other phytoplankton (black) at EI (a), EI_R (b), LI (c), and PI (d). Numbers associated with individual series indicate the year-day of the cast; parentheses represent days for multiple casts. The highest total phytoplankton concentrations were observed at PI at 1×10^5 cells ml^{-1}, which extends from the surface down to 30 m. Stations EI/EI_R had a subsurface peak in cell abundance between 20-40 m at 5×10^4 cells ml^{-1}. Station LI also had a subsurface maximum in cell abundance of 6×10^4 cells ml^{-1} between 10-30 m. *E. huxleyi* abundance was most concentrated at EI/EI_R with 4×10^3 cells ml^{-1} and least concentrated at PI, ranging from 3×10^2 to 1×10^3 cells ml^{-1} at the depths of highest abundance. (a-d), for each sample, n = 2 technical replicates. [Total observations: a) 24 b) 18 c) 17 d) 24]

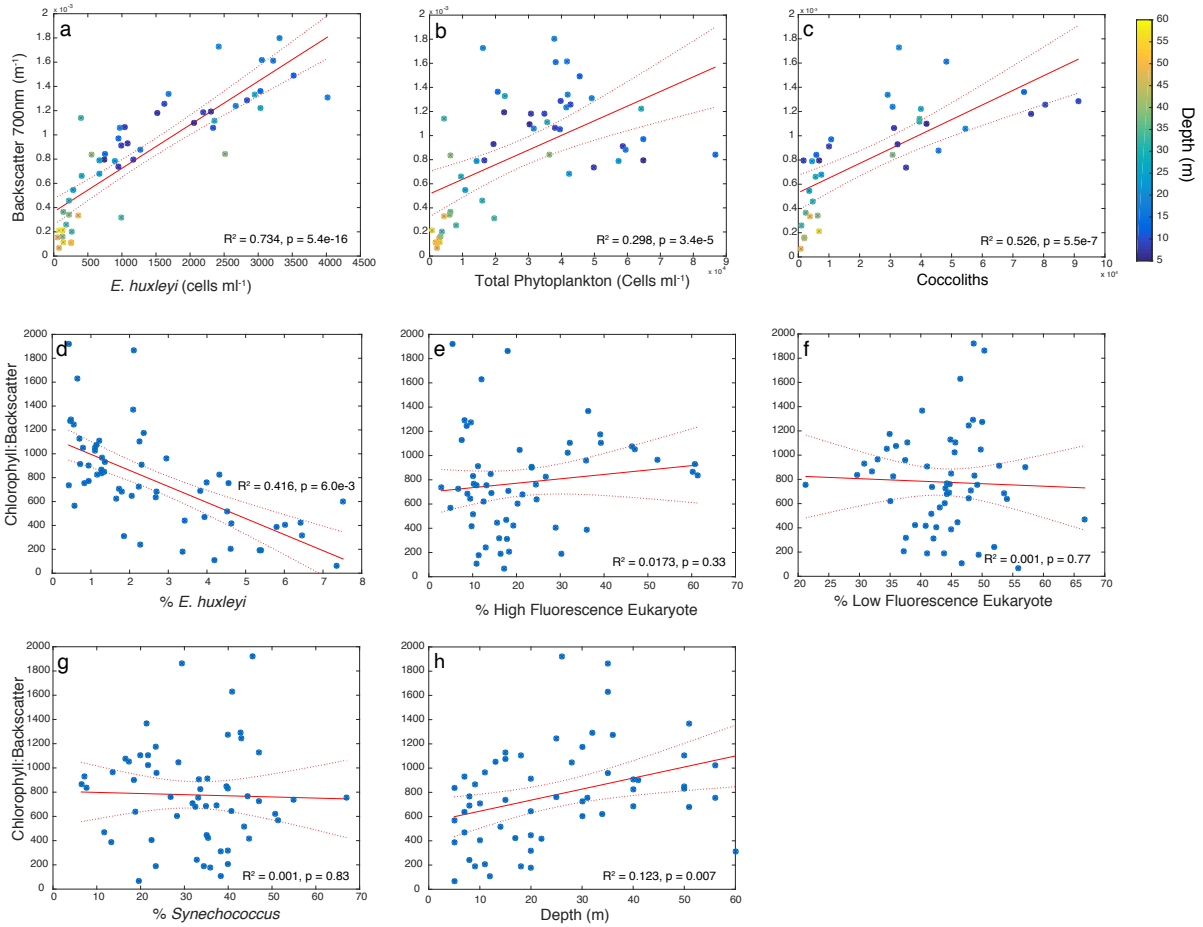

Supplemental Figure 4. Correlation analyses comparing profiling float optical backscatter (700nm) and chlorophyll fluorescence measurements with flow cytometry counts of specific groups of phytoplankton. Both analyses revealed that *E. huxleyi* abundance had a significant impact on these optical parameters. (a) Backscatter has a better relationship to *E. huxleyi* abundance than it does to (b) total phytoplankton abundance despite that *E. huxleyi* only makes up between 0.5-8% of the total cell count (d). (c) Coccolith concentrations also correlated with backscatter but not as well as *E. huxleyi*. Correlations (a-c) are anchored by the deeper measurements with generally low particle numbers having low backscatter. In shallow water measurements, where backscatter is decoupled with depth, the data in (a) show a tighter fit to the regression than in (b), suggesting that *E. huxleyi* cells contribute significantly to the backscatter signal within a mixed population. (d-h) comparison of the relative impacts of cell abundance for discernable subgroups of the community (via flow cytometry) on the chlorophyll:backscatter ratio. (d) *E. huxleyi* had the smallest range in abundance but was the only group that supported a significant relationship to the chlorophyll:backscatter ratio. We recognize that the (e) high fluorescence and (f) low fluorescence containing eukaryote groups are phylogenetically broader than *E. huxleyi* but they are distinguished by their similar chlorophyll fluorescence and side scatter properties. (g) *Synechococcus* was

numerically dominant in many measurements but had a negligible influence on chlorophyll:backscatter. (h) Depth showed a small but positive correlation with chlorophyll:backscatter likely influenced by photoacclimation of cells to lower light at depth. For all panels, solid lines indicate linear regression line; dotted lines indicate 95% confidence intervals. For (a-b), n = 51 observations; (c-h), n = 57 observations.

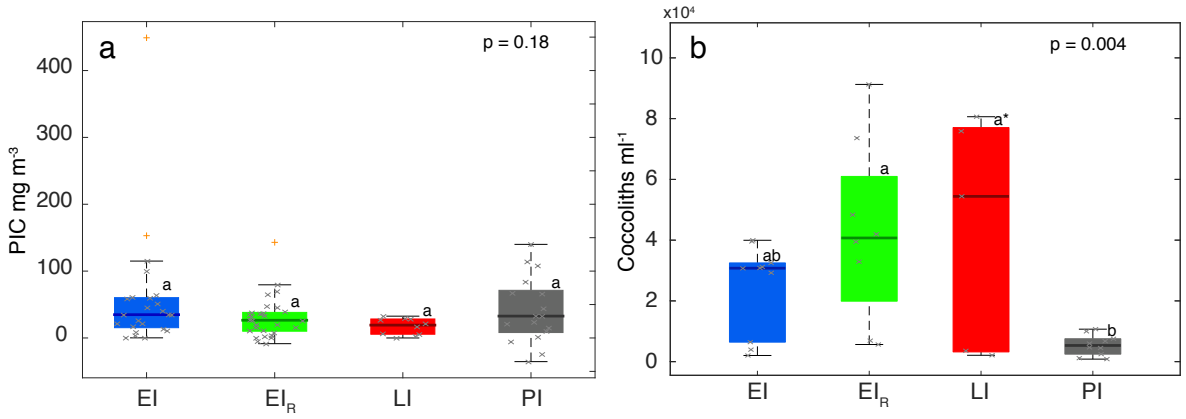

Supplemental Figure 5. (a) Particulate inorganic carbon (PIC) concentrations in the upper 50 m at EI (blue), EI_R (green), LI (red), and PI (gray). No significant differences were observed between stations, with all showing elevated concentrations of PIC. This corroborates with satellite PIC measurements, with elevated PIC observed at each of the water masses (see Figure 1). (b) Free coccolith counts revealed a significantly greater number at EI_R and LI compared to PI. This is in line with the relatively low optical backscatter (B_b) observed at PI (Figure 3). Seeing as calcite-specific scattering is highest for coccolith size particles [1], higher free coccolith concentrations may inflate the B_b signal while PIC concentrations are comparable to areas with lower B_b. *Coccolith samples at LI were only collected at the initial station occupation and not final occupation and, therefore, only reflect the initial optical properties. Box bounds denote 25% and 75% quantiles around the median (thick line). Vertical capped lines indicate max and min data values. Outliers indicated with (+). Letters above boxes denote statistically different groups based on ANOVA. Gray x indicate individual data points. For (a): EI, n = 24; EI_R, n = 29; LI, n = 10; PI, n = 17 station replicates. For (b): EI, n = 10; EI_R, n = 8, LI, n = 5; PI, n = 10 station replicates. [Pairwise comparisons – (a-b) EI:EI_R, EI:LI, EI:PI, EI_R:LI, EI_R:PI, LI:PI a} p = 0.27, 0.22, 0.74, 0.92, 0.93, 0.73 b} p = 0.33, 0.42, 0.22, 0.99, 0.0068, 0.018]

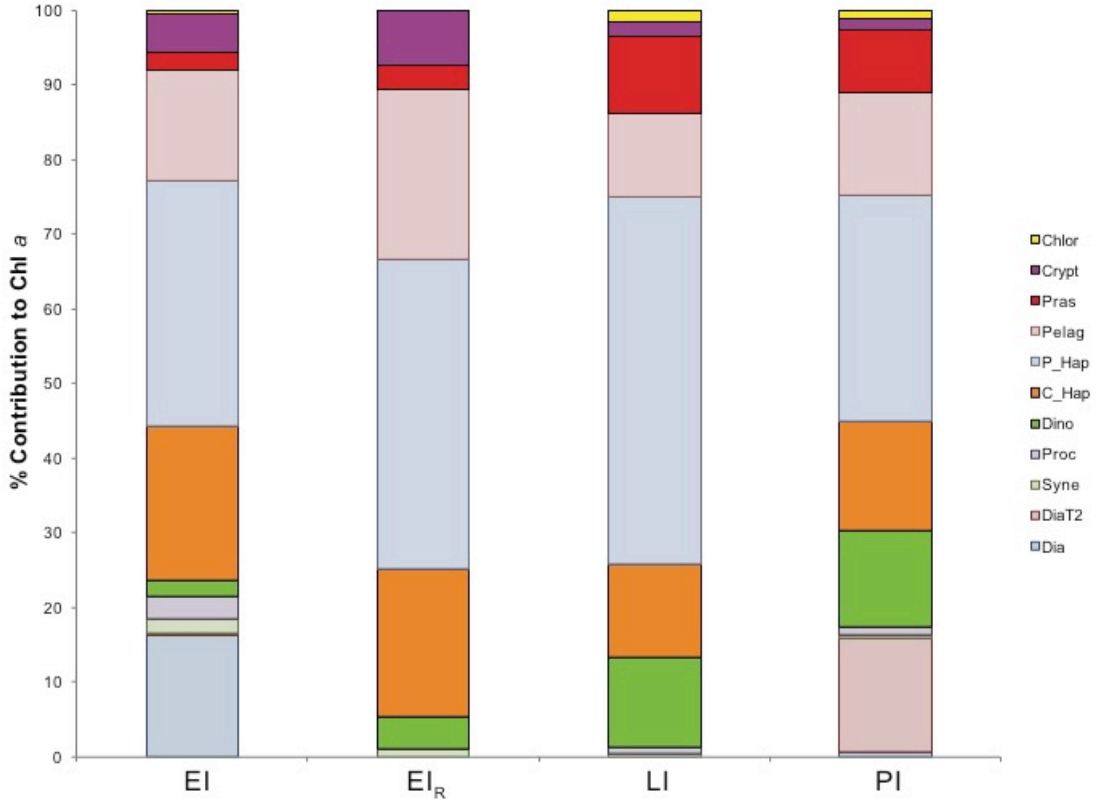

Supplemental Figure 6. The relative contribution of different phytoplankton taxa to total chlorophyll *a* (% contribution to Chl *a*) at EI, EI_R, LI, and PI, as assessed by HPLC-based CHEMTAX . The percent contribution value is normalized to the averaged pigment samples from 0-60 m for each bloom feature. LI and PI stations feature a higher Chl *a* contribution from prasinophytes, chlorophytes, diatoms, and dinoflagellates, while coccolithophore-like haptophytes are less abundant, which may indicate taxa succession. [Chlor –chlorophytes; Crypt – cryptophytes; Pras – prasinophytes; Pelag – pelagophytes; P_Hap – *Phaeocystis* like haptophytes; C_Hap – coccolithophore like haptophytes; Dino – dinoflagellates; Proc – *Prochlorococcus*; Syne – *Synechococcus*; DiaT2 (Type 2) and Dia –diatoms]. In order EI-PI, *n* = 20, 26, 12, 14 station replicates.

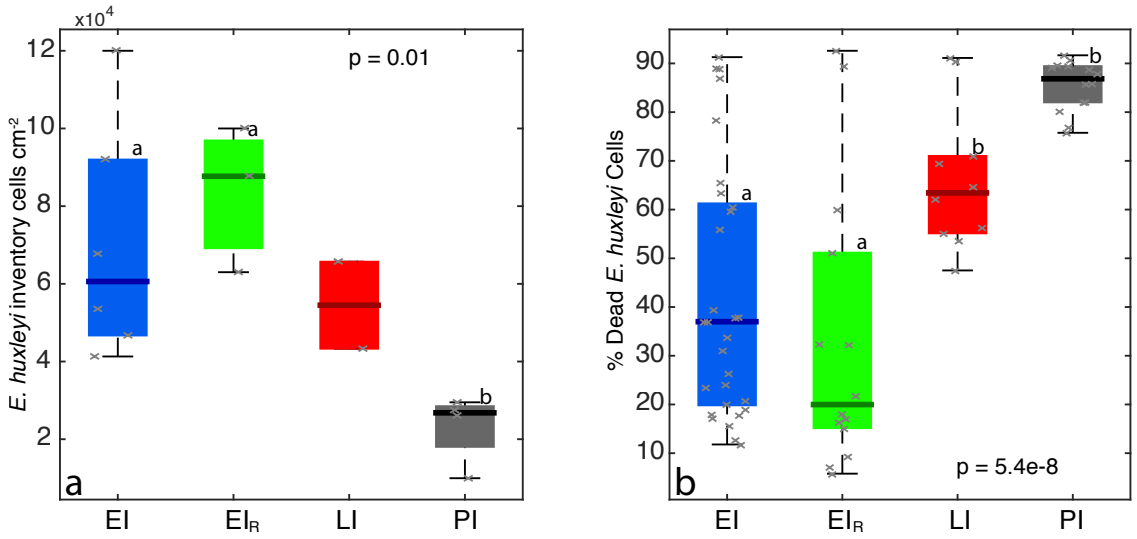

Supplemental Figure 7. Box and whisker plots of water column inventory of *E. huxleyi* cells and the corresponding fraction of dead cells. (a) Water column inventory of *E. huxleyi* cells per cm² from the surface down to 150 m at EI (blue), EI_R (green), LI (red), and PI (black), using flow cytometry data from Supplemental Figure 3. Inventories were most abundant at EI/EI_R and least abundant at PI ($p<0.05$). (b) Fraction of *E. huxleyi* cells positively stained with SYTOX Green, indicating the percentage of dead cells within each feature. SYTOX Green is a charged, DNA intercalating stain that only stains the DNA of operationally dead cells (i.e., those with compromised membranes). Mean mortality was lowest at EI_R (33%) and EI (42%), and progressively increased at LI (66%) and PI (85%), where most *E. huxleyi* cells were dead ($p<0.001$). Box bounds denote 25% and 75% quantiles around the median (thick line). Vertical capped lines indicate max and min data values. Letters above boxes denote statistically different groups based on ANOVA. For (a), n = 6, 3, 2, 4 station replicates. Gray x indicate individual data points. No statistic on LI with n = 2. For (b), n = 29, 14, 10, 14 station replicates, respectively. [Pairwise comparisons – (a) EI:EI_R, EI:PI, EI_R:PI, p = 0.71, 0.029, 0.019; (b) EI:EI_R, EI:LI, EI:PI, EI_R:LI, EI_R:PI, LI:PI, p = 0.65, 0.026, 9.9e-7, 0.0048, 4.7e-7, 0.17]

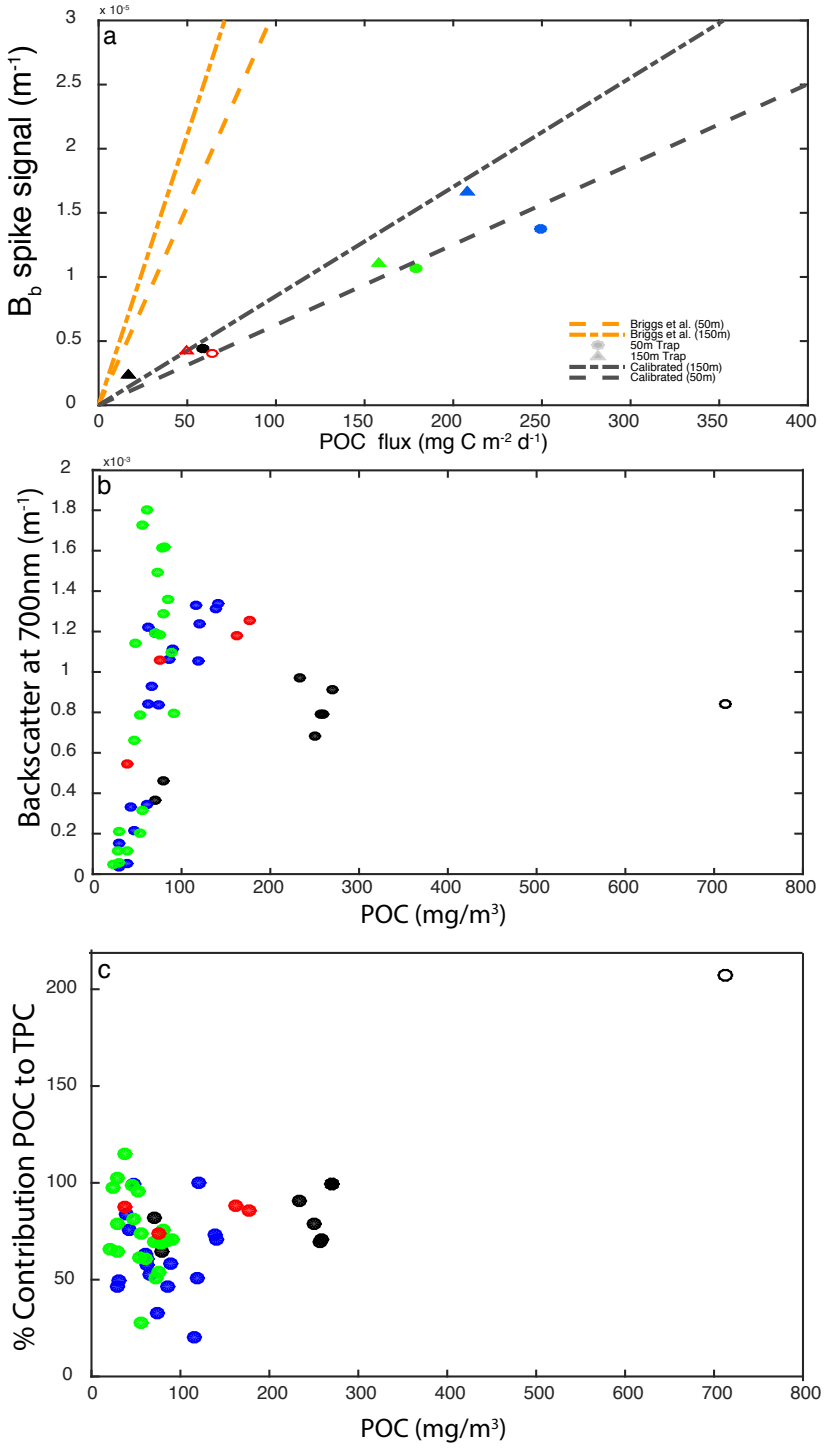

Supplemental Figure 8. Relationship between total carbon flux and backscatter spike signal. The measured particulate organic carbon (POC) flux rate measurements at 50 m (circles) and 150 m (triangles) was compared to the spike aggregate signal at those respective depths at EI, EI_R, and PI. Briggs et al. explored using the spike signal as an estimate for aggregate POC flux using equation [(2); rearranged below] using a 75 m d^{-1} sinking rate, terms that accounted for the ratio

of POC to optical backscatter (B_b) signal [35400 mg C m^{-2}], and a correction for organic carbon loss in a particle during sinking [$(z/100m)^{-0.28}$], where *z* is the depth of the measurement[2]. The Briggs et al. estimates for the relationship between POC and the spike signal at 50 m and 150 m are shown in orange. Our data depart from this relationship between POC and the B_b spike signal, likely based on several factors. First, the significant contribution of PIC to the total particulate carbon (TPC) in our systems would change the relationship between POC and the B_b spike signal, as PIC would then account for a portion of the signal (PIC is assumed to inflate the B_b signal and thus lower the ratio). (b-c) The % contribution of POC to TPC varied among samples and stations, likely explaining some of the variability observed in the POC:B_b relationship (c). EI and EI_R commonly exhibited very low % POC within observations. However, using Eq. (2), a lower POC:B_b ratio would increase the slope observed in (a) rather than decreasing it to one comparable to our data. A second possibility is that differences in the calibration in B_b sensor between our profiling floats and the platform used in the Briggs et al. study. We tested this by using an average ratio of POC:B_b from our data (175443 mg C m^{-2}) in Eq. (2). The result is shown above with the calibrated 50 m and 150 m regression lines (gray). Of note, the data not only follow the calibrated regressions more closely, but the 150 m data also depart from the 50 m as predicted by Eq. (2). We then used the calibrated Eq. (2) to estimate the POC flux at LI, where no sediment traps were deployed, based on the B_b spike signals observed at 50 m and 150m, yielding estimates of 64 and 49 mg C m^{-2} d^{-1}, respectively (a; hollow red shapes). For (a-c) scatter plots are colored by station with EI (blue), EI_R (green), LI (red), and PI (black). In (a) data points represent average values of flux and spike signal. For spikes, n = 25, 25, 31, 24 binned values at EI, EI_R, LI, and PI, respectively, for both 50 and 150m. For all POC flux, n = 3. In (b-c), hollow data outlier with extreme POC value was removed from analysis; *n* = 51 observations.

B_b spike signal = aggregate POC flux/(35400 mg C m^{-2} × 75 m d^{-1} × $(z/100m)^{-0.28}$) **(2)**

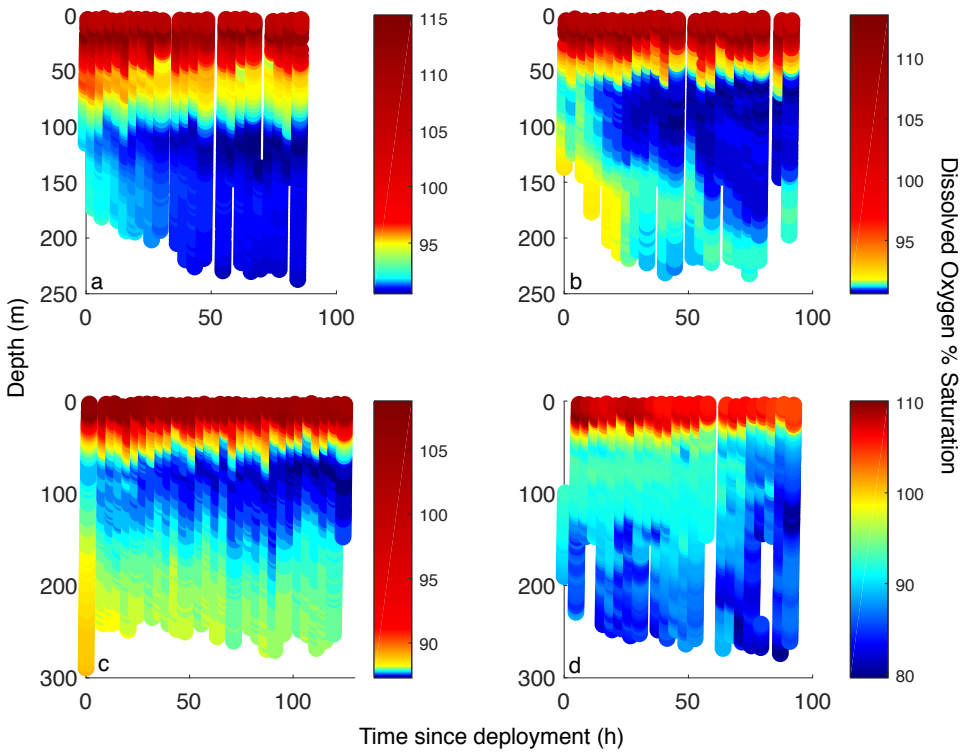

Supplemental Figure 9. Dissolved oxygen concentrations (DO; % saturation) measured during profiling float deployments for EI (a), EI_R (b), LI (c), and PI (d) water masses. Sub-surface minimum layers in DO were observed between 50 and 150 m for EI, EI_R, and LI. Additionally, steady decreases were observed over the observation time at depths below the euphotic zone (~50 m across all stations). Color bars at EI, EI_R, and LI are adjusted to highlight the small sub-euphotic decreases in DO over the deployment periods. For individual data points, *n* =1 technical replicate.

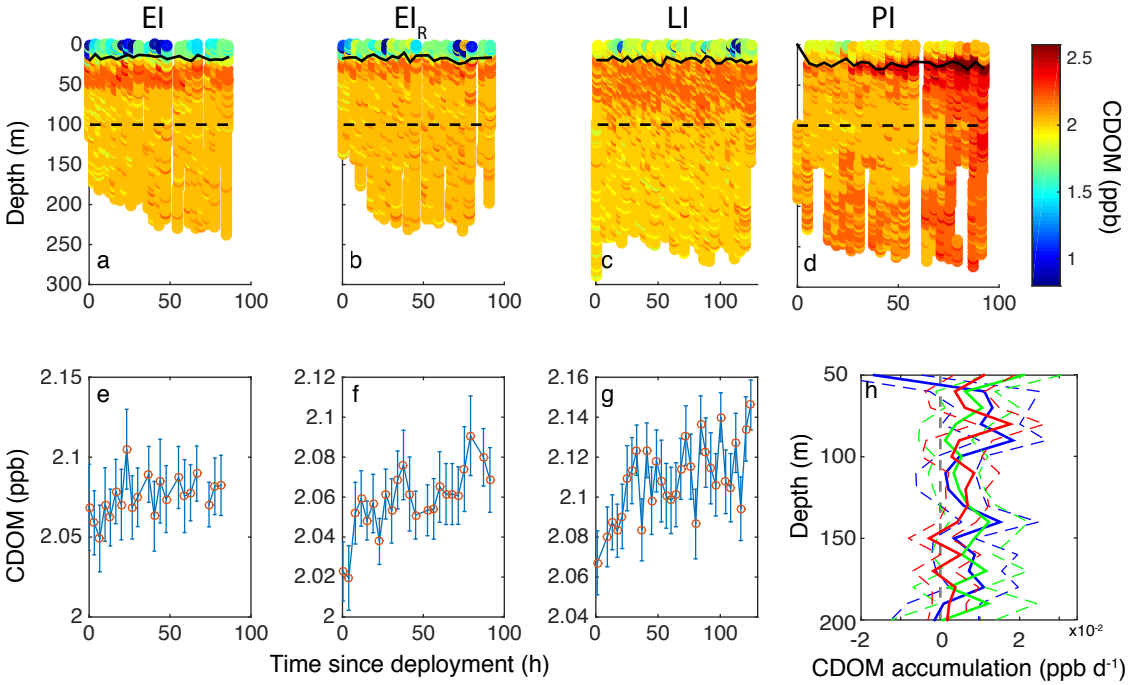

Supplemental Figure 10. Water column profiles of fluorescent chromophoric dissolved organic matter (CDOM) at EI (a), EI_R (b), LI (c), and PI (d) over periods of profiling float deployments. Solid black lines indicate the depth of the pycnocline, as measured by the maximum change in density over change in pressure. Dashed black lines indicate the 100 m depth horizon. (e-g) Changes in the average CDOM concentration from the pycnocline to 100 m (error bars denote ± 1 SE). Virus infection and cell lysis has previously been linked to releases of CDOM, but accumulation is not observed in all studies [3,4]. The elevated fluorescent CDOM in the photobleached surface water observed at LI and PI, compared to EI and EI_R, suggests recent production of CDOM at those features. Vertical mixing between the surface and sub-surface layer is likely not an explanation for higher surface CDOM at LI because of increases in the subsurface layer CDOM (g); rather, it would show decreases if it was diluted by the surface water. Due to mixing sub-surface water masses, PI was not included in this analysis. (h) CDOM accumulation rates are small and positive at EI (blue), EI_R (green) and LI (red). Dashed lines indicate upper and lower 95% confidence intervals. Though it is unclear what processes are contributing to CDOM production—whether phytoplankton can directly exude CDOM during lysis[5] or there is a necessary intermediate after viral lysis and release of DOM to produce CDOM[3]— it appears CDOM production may occur throughout infected blooms. For data points in (a-d), n = 1 technical replicate. For (e-g), min n = 19, max n = 31 data points contribute to each average. For (e-h) n = 25, 25, 31, 24 profiles for EI, EI_R, LI, PI, respectively.

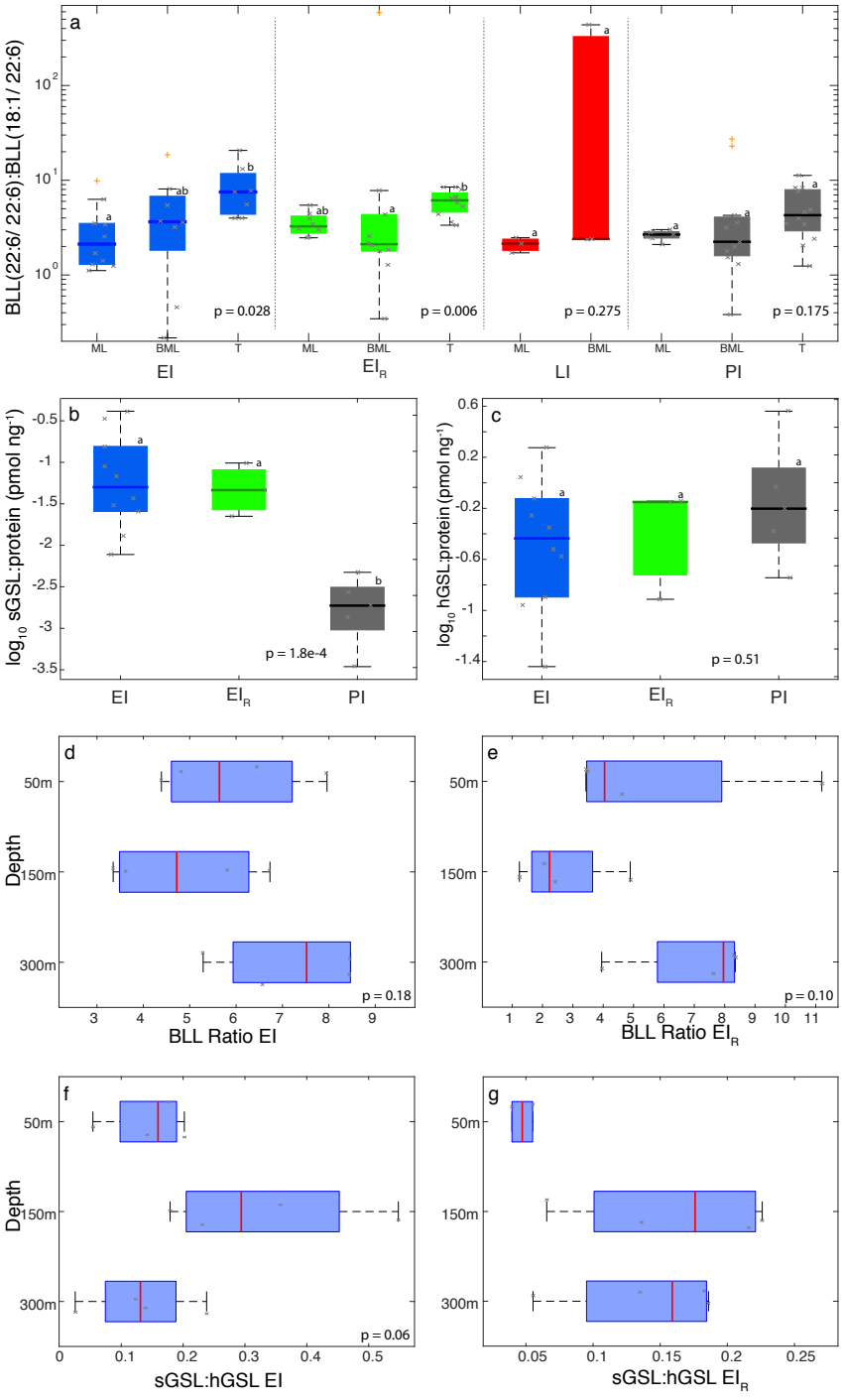
a
BLL(22:6/ 22:6):BLL(18:1/ 22:6)
p = 0.028
p = 0.006
p = 0.275
p = 0.175
ML
BML
T
EI
EI$_R$
LI
PI
b
log$_{10}$ sGSL:protein (pmol ng^{-1})
p = 1.8e-4
c
log$_{10}$ hGSL:protein (pmol ng^{-1})
p = 0.51
d
Depth
50m
150m
300m
p = 0.18
BLL Ratio EI
e
p = 0.10
BLL Ratio EI$_R$
f
p = 0.06
sGSL:hGSL EI
g
sGSL:hGSL EI$_R$

Supplemental Figure 11. Observations of infectivity lipid ratios at individual stations. (a) The betaine-like lipid BLL(22:6/ 22:6) to BLL(18:1/ 22:6) ratio at individual stations had median values that were consistently higher in sediment trap material than in water column material. Significant differences between the mixed layer and trap material ratios were observed at EI, while at EI_R, only the water below the mixing layer differed significantly from the trap material (Kruskal-Wallis ANOVA). There were no significant differences between mixed layer (ML), below mixed layer (BML), and trap (T) ratios at PI. No traps were deployed at LI and there was no difference above and below the mixing layer depth. (b-c) The biomass-normalized ratio of sialic acid glycosphingolipid (sGSL) (sGSL:protein) was greatly elevated in trap material at EI and EI_R compared to PI (ANOVA). These differences were not observed for biomass-normalized ratios of host glycosphingolipid (hGSL) demonstrating the preferential enrichment of sensitive, *E. huxleyi* cells in the traps at EI and EI_R. For a-b, letters above boxes denote statistically different groups. (d-e) BLL ratios and (f-g) sGSL:hGSL ratios in sediment trap material collected at 50 m, 150 m, and 300 m were statistically indistinguishable between depths (ANOVA). Taken together, data from panels (d-g) are consistent with sinking particles being derived from the same infected surface source populations at EI and EI_R with high sinking rates. For all plots, upper and lower box bounds denote 25% and 75% quantiles around the median (thick line). Vertical capped lines indicate max and min data values. Outliers indicated with (+). Gray x indicate individual data points. For (a), n = 10, 8, 7,8 10, 12, 3, 3, 7, 11, 12 environmental replicates; For (b-c), n = 10, 3, 5 station replicates; for (d-f), n = 4, 4, 4 environmental replicates; For (g), n = 2, 4, 4 environmental replicates, respectively. No statistic on (g) with n = 2. [Pairwise comparisons – (a: EI,EI_R,PI) ML:BML, ML:T, BML:T, EI} p = 0.69, 0.02, 0.18 EI_R} p = 0.79, 0.073, 0.0066 PI} p = 0.99, 0.27, 0.24 (b-c) EI:EI_R, EI:PI, EI_R:PI b} p = 0.96, 1.6e-4, 0.0037 c} p = 0.99, 0.43, 0.57 (d-g) no pairwise comparison]

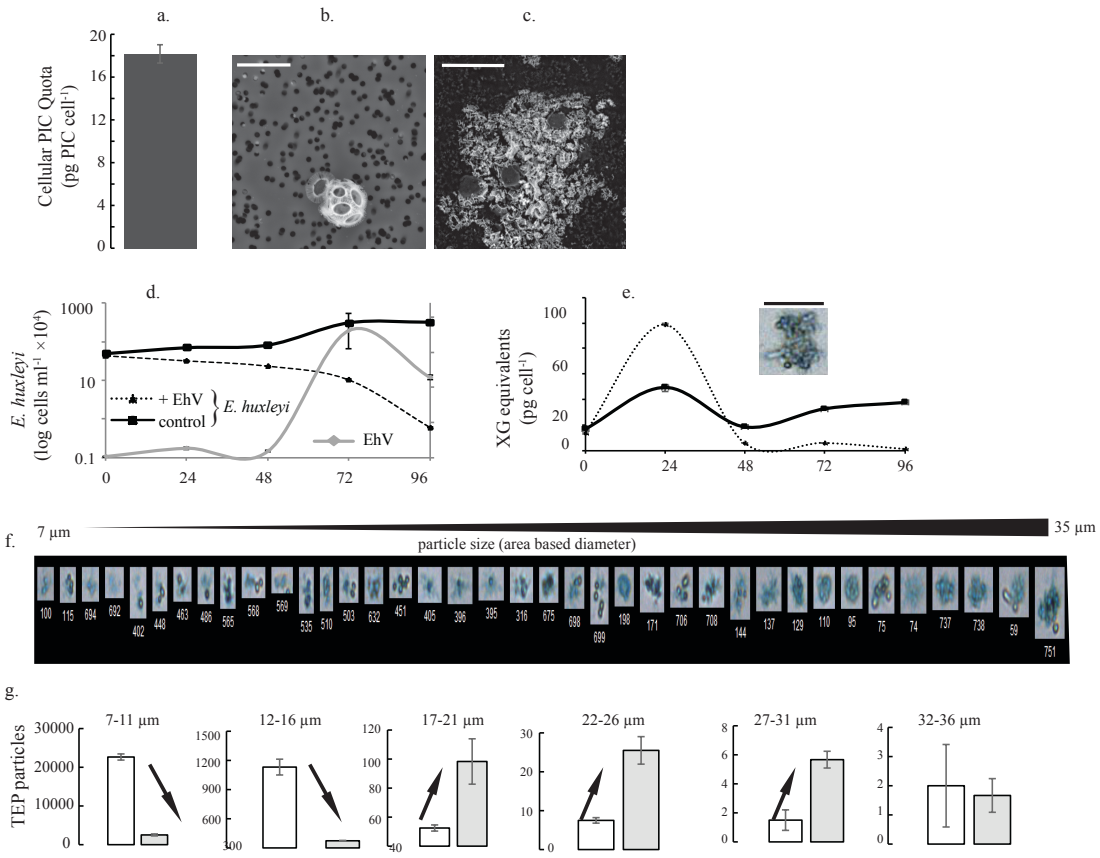

Supplemental Figure 12. EhV infection of calcified *E. huxleyi* triggers transparent exopolymeric particle (TEP) and particle production. (a) Cell-associated particulate inorganic carbon quota for *E. huxleyi* DHB607. Error bars denote ± SD around the mean. (b-c) Scanning electron microscopy (SEM) images of calcified DHB607 as a single cell (b) and aggregated particle during virus infection (c); scale bars correspond to 5 µm and 8 µm, respectively. (d) Infection dynamics of host and virus abundance for infected and uninfected DHB607 cells. Average host abundance (± SD from biological triplicates) during infection with EhV99B1 (dotted lines) and for virus free control (solid lines), along with corresponding EhV99B1 abundance for infected treatment, as measured by flow cytometry (see Methods). (e) Comparative dynamics of TEP production for data shown in panel (d). Plots show the dynamics of TEP production (average ± SD) for DHB607 cells in the presence (dotted lines) and absence (solid lines) of EhV99B1 (left panels) over 96 h infection period. TEP concentrations are expressed in xanthum gum (XG) equivalents. Note the increse in cellular TEP production during early infection dynamics, which is not due to cell lysis (which was observed 72 hours post infection, hpi). *Inset*: FlowCam imaged particle from EhV99B1-infected DHB607 culture (scale bar= 30 µm). (f) A representative snapshot Alcian Blue-stained TEP-containing aggregates from *E. huxleyi* DHB607, as imaged by FlowCam. Imaged aggregates were sorted based on the average blue to average green ratio, followed by an area based diameter (ABD), which is automatically calculated by the FlowCam software. The smallest aggregates are on the left while the largest aggregates are on the right (range of

7-35 μm shown) (g) Patterns in the number of aggregates within arbitrarily-defined size classes for *E. huxleyi* DHB607 during infection with EhV99B1. Alcian Blue-stained TEP-containing aggregates (like those pictured in inset of panel (e) were imaged by FlowCAM and sorted based on area based diameter, which is automatically calculated by the FlowCam software. Size bin ranges are indicated above each panel. Bars represent the average number of aggregates (± SD for biological triplicates) within each size range at the end of the experiment for uninfected control (white) and EhV99B1-infected (gray) cultures. Arrows indicate the respective shift in aggregate number. Note the increase in larger aggregates in infected cells relative to control. For a, d, e, and g, n = 3 biological replicates.

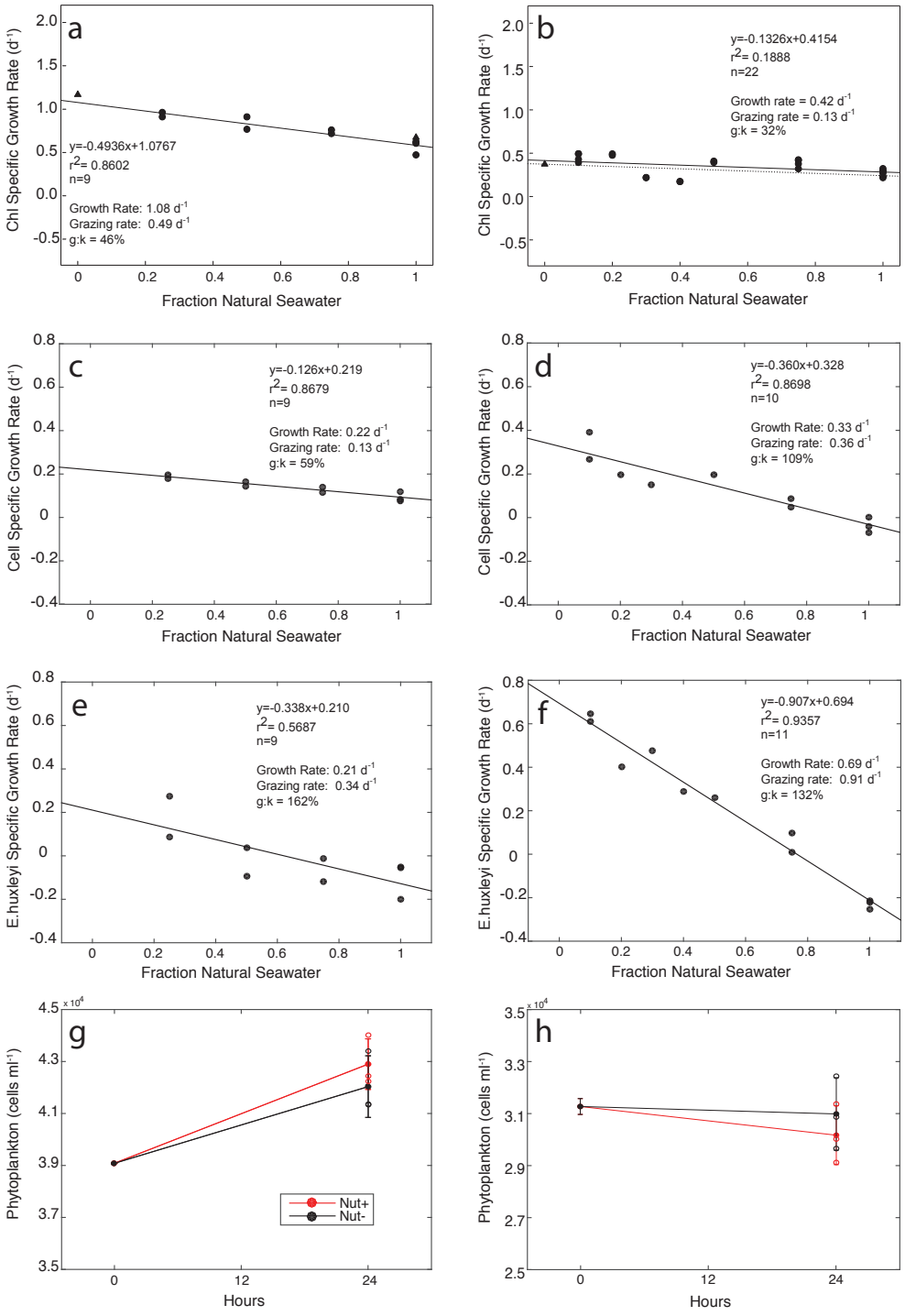

Supplemental Figure 13. Community and *E. huxleyi* specific growth and grazing rates derived from Landry-based[6] dilution experiments performed at EI (a, c, e, g)

and EI_R (b, d, f, h). (A-B) Using the classic chlorophyll based measurement of growth rate, linear projection to community growth in the absence of grazers shows positive growth rates over the 24 h incubation period for both EI and EI_R. Grazing was relatively elevated at EI in comparison to EI_R. (c-d) While cell-specific community growth rates also showed generally positive growth rates in the absence of grazing, cell specific grazing pressure was higher at EI_R than EI. These differences may be explained by selective retention of phytoplankton during chlorophyll filtration (inefficient retention of small, < 0.7 μm, picophytoplankton such as *Synechococcus* onto GF-F filters) or by preferential grazing on particular prey species. (e-f) *E. huxleyi* specific grazing was elevated (almost three times higher) at both EI and EI_R in comparison to community grazing rates. (g-h) Some incubations were spiked with ammonia, phosphate, and silica to alleviate the possible impact of nutrient limitation on cells in dilution experiment. Statistically indistinguishable changes in cell concentration over 24 h for incubations with (Nut+; red) and without (Nut-; black) nutrient argue that resident populations were not nutrient limited (Student's T test, $p = 0.38, 0.47$, respectively for g and h T24). For (g); T0, $n = 2$; T24, $n = 3$ biological replicates. For (h); $n = 3$ biological replicates. Open circles indicate individual data points. Error bars represent ± 1 SD around the mean.

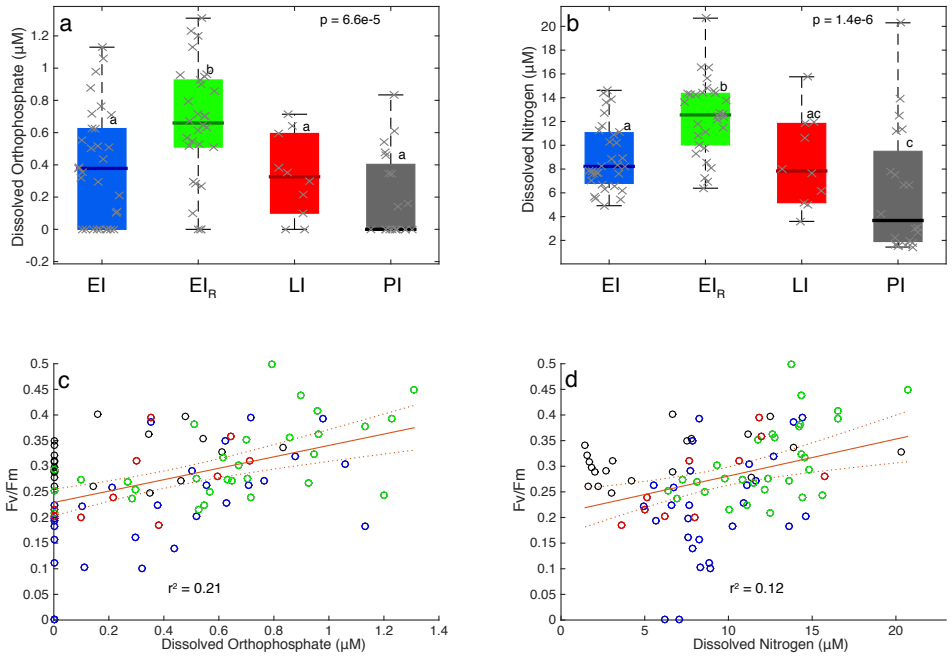

Supplemental Figure 14. (a) Orthophosphate and (b) nitrogen concentrations in the upper 50m at EI (blue), EI_R (green), LI (red), and PI (gray). EI/EI_R and LI concentrations were similar to or higher than those observed during an *E. huxleyi*-dominated mesocosm bloom experiment[7], suggesting nutrients were not limiting growth. PI had significantly lower dissolved nitrogen concentrations but also had the highest phytoplankton community abundance (Figure S1). Only weak correlations were observed between photosynthetic quantum yield of photosystem II (F_v/F_m) and respective concentrations of (c) dissolved orthophosphate or (d) dissolved nitrogen at all stations. It was noteworthy that F_v/F_m measurements for PI populations were all >0.2, suggesting the resident phytoplankton community encountered limited nutrient stress. For (a-b), box bounds denote 25% and 75% quantiles around the median (thick line). Vertical capped lines indicate max and min data values. Gray x indicate individual data points. Letters above boxes denote statistically different groups based on ANOVA. For (a-d), in order, sample size is n = 31, 30, 10, 20 station replicates. For (c-d), dashed lines represent 95% confidence bounds around the regressions. Orthophosphate and nitrogen values shown in (c-d) are the same as those represented in (a-b).

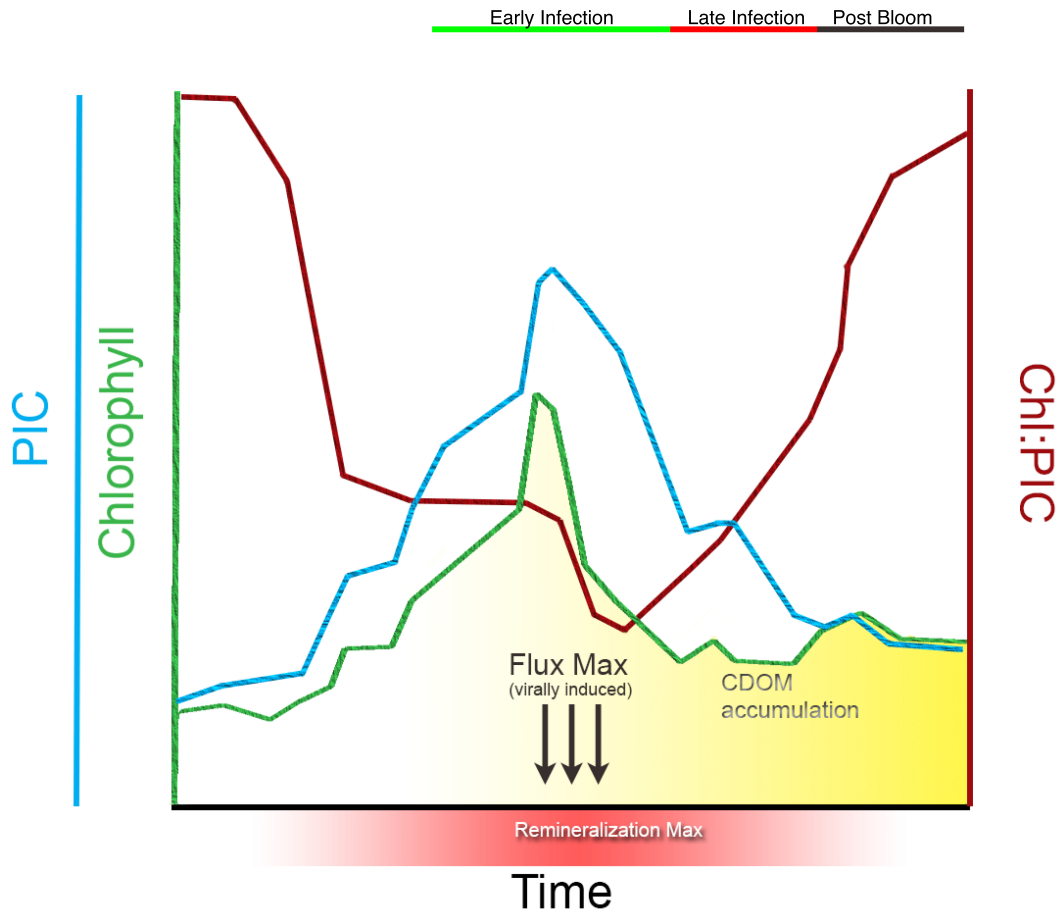

Supplemental Figure 15. Conceptual model showing the expected dynamics of an infected *E. huxleyi* bloom, based on satellite hindcasting over the lifespan of the LI population and our collective *in situ* observations at all three stations. The LI station had a chlorophyll (Chl) peak four times higher than EI/EI_R and two times higher particulate inorganic carbon (PIC) reflectance, consistent with a very large coccolithophore bloom. With atmospheric conditions allowing for comprehensive satellite imagery, this bloom served as a scaffold upon which to layer and interpret the different stages of EhV infection with EI/EI_R representing the peak of the bloom, LI representing late stages of termination, and PI following the termination as Chl recovers. Through the model bloom initiation seen above, increasing Chl and PIC (with a greater change in magnitude of PIC) drive down the Chl:PIC ratio, as observed by remote and *in situ* sensing instruments. Induced production of aggregated particles (via TEP production) during early infection coupled with enhanced grazing of infected cells become prominent controls on *E. huxleyi*

accumulation, in turn increasing particle flux from the surface ocean, becoming maximal around the peak of the bloom. The high particle flux is accompanied by elevated remineralization of the sinking particulate matter in the mesopelagic. Following the peak of the bloom, the Chl *a*:PIC ratio decreases further, with the removal of PIC lagging behind decreases in Chl, likely due to enhanced presence of high-scattering, free coccoliths before the ratio increases into late infection upon phytoplankton succession. Flux rates relax through the termination of the bloom. CDOM accumulation rate increases through the termination of the bloom and into the post-bloom, with succeeding phytoplankton increasing Chl at the as PIC continues to diminish.

SUPPLEMENTAL TABLES

Supplemental Table 1. Depth integrated water column respiration from 50-150 m derived from optical measurements of dissolved oxygen utilization and direct bottle based measurements of microbial community respiration[8]. The statistical uncertainty of direct measurements was calculated using the bootstrap method described in Collins et al.[1]. Optical measurements closely follow the direct observation measurements at EI and EI_R. Confidence intervals represent ± 1 SD of the mean.

50-150m	Optically derived Depth-integrated water column respiration	Direct observation Depth-integrated water column respiration [1]
Station	**(mg C m^{-2} d^{-1})**	**(mg C m^{-2} d^{-1})**
EI	669.0	887.9 ± 456.2
EI_R	665.9	835.0 ± 629.0
LI	165.8	--
PI	--	465.2 ± 182.1

Supplemental Table 2. Correlations for PIC with GSL species. sGSL explain 65% of the variability in PIC sinking flux rate while hGSL and vGSL had negligible explanatory power. This suggests that material from susceptible *E. huxleyi* makes up a significant fraction of the coccolithophore and coccolith export. P values obtained by ANOVA.

	sGSL:PIC*	hGSL:PIC	vGSL:PIC
Regression Coefficient	0.019	1.639E-04	0.009
Intercept	18.307	45.594	46.975
R Square	0.650	0.008	0.002
P-value	1.47E-08	0.604	0.791

*with the removal of one highly leveraging outlier

Supplemental Table 3. **Deck-board seawater incubations.** Flow cytometery measurements of *E. huxleyi* and total phytoplankton populations measured over 2-3 d in seawater collected at 8 m depth from EI_R. TEP concentrations were also measured at each time point. Control incubations were maintained at 20% surface PAR while the low light incubation was maintained at 1% surface PAR.

Incubation	Date	Group	hours	*E. huxleyi* Average ± 1 SD (cells ml^{-1})		Total Phytoplankton Average ± 1 SD (cells ml^{-1})		TEP Average ± 1 SD (OD L^{-1})	
	7/10/12	Control	20	1422.06	± 164.06	29079.49	± 29.64	-3.82	± 0.47
EI_R 1	7/11/12		41	1651.64	± 41.08	34123.73	± 1180.66	-6.03	± 4.90
	7/12/12		66	1871.93	± 203.13	24402.52	± 1284.64	33.51	± 4.45
	7/12/12	Low Light	31	807.96	± 64.14	25773.77	± 1084.19	4.61	-
EI_R 2	7/13/12		53	924.52	± 12.20	24137.39	± 743.47	50.58	± 1.23
	7/12/12	Control	31	1190.53	± 51.29	29903.26	± 1514.31	12.12	-
	7/13/12		53	1469.73	± 273.49	27766.18	± 884.03	41.27	± 7.14

REFERENCES

1 Balch, W. M., Kilpatrick, K. A., Holligan, P., Harbour, D. & Fernandez, E. The 1991 coccolithophore bloom in the central North Atlantic. 2. Relating optics to coccolith concentration. *Limnology and Oceanography* **41**, 1684-1696 (1996).

2 Briggs, N. *et al.* High-resolution observations of aggregate flux during a sub-polar North Atlantic spring bloom. *Deep Sea Research Part I: Oceanographic Research Papers* **58**, 1031-1039 (2011).

3 Balch, W. M. *et al.* Fundamental changes in light scattering associated with infection of marine bacteria by bacteriophage. *Limnology and oceanography* **47**, 1554-1561 (2002).

4 Rochelle-Newall, E. *et al.* Chromophoric dissolved organic matter in experimental mesocosms maintained under different pCO2 levels. *Marine Ecology Progress Series* **272**, 25-31 (2004).

5 Castillo, C. R., Sarmento, H., Alvarez-Salgado, X. A., Gasol, J. M. & Marraséa, C. Production of chromophoric dissolved organic matter by marine phytoplankton. *Limnology and Oceanography* **55**, 446-454 (2010).

6 Landry, M. & Hassett, R. Estimating the grazing impact of marine micro-zooplankton. *Marine biology* **67**, 283-288 (1982).

7 Kimmance, S. A., Allen, M. J., Pagarete, A., Martínez, J. M. & Wilson, W. H. Reduction in photosystem II efficiency during a virus-controlled Emiliania huxleyi bloom. *Marine Ecology Progress Series* **495**, 65-76 (2014).

8 Collins, J. R. *et al.* The multiple fates of sinking particles in the North Atlantic Ocean. *Global Biogeochemical Cycles* **29**, 1471-1494 (2015).